AIAA SciTech Forum
12-16 January 2026, Orlando, FL
AIAA SCITECH 2026 Forum

10.2514/6.2026-1927

Statistical Characterization of Transient Energy Growth in Rayleigh-Taylor Instability under Multimodal Perturbations

Marildo Kola*
University of Michigan, Ann Arbor, MI, 48109

Daniel Israel†
Los Alamos National Laboratory Michigan SPARC, Ann Arbor, MI. 48104

Aaron Towne‡
University of Michigan, Ann Arbor, MI, 48109

A novel statistical framework developed by Ref. [1] is employed and extended to examine how initial conditions influence the linear evolution of the Rayleigh–Taylor instability. The analysis focuses on the evolution of the mean energy for two representative classes of initial perturbations. The first class, based on a Gaussian spatial correlation, reveals a time delay in the onset of instability growth and a non-monotonic dependence of this delay on the perturbation correlation length. This behavior suggests a low-pass-filter-like selection of modes governing the evolution of the mean energy. The second class consists of perturbations formed as linear combinations of Fourier modes with random phase shifts and amplitudes drawn from a prescribed spectrum. For this case, an analytical expression for the mean energy growth is derived, linking the spectral content of the initial perturbations to the temporal evolution of the energy through the initial spectral amplitudes. This formulation enables direct comparison with ensembles of three-dimensional direct numerical simulations demonstrating both the framework's predictive capability and the limitations imposed by the problem's non-autonomous nature. Finally, the effects of viscosity and density stratification are analyzed, showing how these factors modify the time-delay mechanism and influence the early-stage evolution of the instability.

I. Introduction

The Rayleigh–Taylor instability (RTI) arises when two fluids of different densities experience an acceleration misaligned with their density stratification. Ref. [2] conducted the initial investigations of this phenomenon, and since then, RTI has been identified as a fundamental mechanism in numerous natural phenomena, such as core-collapse supernovae [3] and the early evolution of rarefied bubbles in cooling-flow clusters of galaxies [4]. From an engineering standpoint, understanding RTI is essential for inertial confinement fusion (ICF) [5], where it is the leading cause of efficiency loss. During the ablation phase of implosion, surface imperfections are amplified by RTI, as the low-density ablated material exerts a force on the high-density shell. This amplification distorts the imploding shock, transmits perturbations to the shell, and induces rippling of the interface, ultimately hindering ignition [6]. Therefore, understanding the influence of initial disturbances on RTI evolution is critical for designing capsules that can delay its onset [7].

The primary physical mechanism driving the Rayleigh–Taylor instability is the generation of baroclinic torque due to the misalignment between density and pressure gradients. This torque induces vorticity around the perturbed interface, leading to system instability [8], where the resulting flow undergoes linear and nonlinear development, eventually transitioning to turbulence.

The comprehensive review by Ref. [9] shows how effort has been directed toward single-mode analysis to understand the effect of initial conditions, particularly within the framework of linear stability theory. In such analysis, a

*Graduate Students, Department of Aerospace Engineering, AIAA Student Member, marildo@umich.edu
†Scientist, Continuum Models and Numerical Methods, AIAA Senior Member
‡Associate Professor, Department of Mechanical Engineering, AIAA Senior Member

single-wavelength perturbation is imposed to study its impact; the linear regime justifies this approach through the superposition principle, allowing independent analysis of each mode. In contrast, multimodal initial conditions have primarily been investigated in the context of late-time flow behavior, with particular emphasis on mixing, and significant research has focused on how various initial conditions affect evolution at each stage [10, 11]. In general, two types of multimodal initial conditions have been considered. In the first type, long-wavelength perturbations are explicitly included in the initial spectrum and have been observed to dominate the late-time growth of the mixing layer [12]. In the second type, the initial spectral content lacks significant low-wavenumber energy. In this scenario, long wavelengths are generated via nonlinear mode coupling. Under these conditions, the memory of the initial conditions is usually lost, leading to a self-similar turbulent regime [13]. More recently, Ref. [14] conducted nearly 500 direct numerical simulations at fixed viscosity, diffusivity, and Atwood number for a specific spectrum of initial conditions under the Boussinesq approximation. Their study analyzed the influence of initial-condition memory across different instability stages using data-driven machine learning techniques, highlighting the high sensitivity of stage transitions to the number of modes included in the response and the significant challenge this poses for modeling the Rayleigh–Taylor transition. It is within this context that the present study has been developed. Specifically, it adopts a novel approach to address the influence of initial conditions on the Rayleigh-Taylor instability. Ref. [1] introduced a new perspective for analyzing transition energy growth and optimal perturbations, enabling statistical examination of disturbance evolution under linear dynamics. This statistical framework was initially formulated for shear flows, where non-modal growth is recognized as the principal mechanism contributing to the transition to turbulence. In particular, it was observed that when random initial conditions perturb the flow, the initial perturbation is rarely optimal as defined by Ref. [15]. As will be shown, this framework is particularly suitable for analyzing the impact of Rayleigh–Taylor initial conditions because it allows the derivation of closed-form expressions that directly relate the statistics of perturbations to the evolution of system energy during the linear stages.

The structure of this work is outlined as follows. Section II introduces the statistical framework through which the Rayleigh–Taylor instability is analyzed and establishes the major notation. Section III discusses the characterization of the initial disturbances, with particular emphasis on how the statistical framework can be leveraged to directly connect the statistical characterization of the incoming perturbations to the evolution of the Rayleigh–Taylor mean energy. The framework is discussed in the most general setting, meaning that, as long as the dynamics are linear, it can be applied to general forms of variable-density governing equations. Section IV introduces and discusses the governing equations used in this study. In particular, the incompressible variable-density model introduced by Ref. [16] and the Boussinesq model will be considered. A brief description of the numerical solver developed to analyze the dynamics is provided in Section V. After discussing the concept of an energy norm in unstably stratified flows in Section VI, results are presented for two types of initial perturbation statistics. The first is a Gaussian isotropic model that represents the simplest perturbation statistics characterized by a single correlation length. The second type of perturbation matches those used in previous direct numerical simulations of Rayleigh–Taylor instability, enabling direct comparison during the linear stage and providing a low-cost means to predict the evolution of three-dimensional disturbances and assess the influence of initial conditions on the dynamics. A direct comparison with numerical ensembles is therefore presented, and discrepancies associated with the non-autonomous nature of the problem are discussed.

II. Methodology

The primary quantity examined in this study is the mean energy growth as introduced by Ref. [1]. This section reviews the main concepts and introduces the notation employed throughout the analysis. Two sets of equations describing the evolution of the Rayleigh–Taylor instability are considered, and a general formulation is therefore presented to characterize mean energy growth independently of the specific set of governing equations. In this work, vectors of continuous and discretized variables will appear; therefore, it is necessary to establish a notation that distinguishes between them. In particular, a vector of continuous variables will be expressed as $\boldsymbol{q}$ while the corresponding discretized quantity will be denoted as $\mathbf{q}$.

In general, the governing equations describing the evolution of variable-density flow can be expressed in compact form as

$$\frac{\partial \boldsymbol{q}}{\partial t} = \mathcal{N}(\boldsymbol{q}(\boldsymbol{x}, t)). \tag{1}$$

Here, $\boldsymbol{q}$ represents the state vector of flow variables, and $\mathcal{N}$ denotes the corresponding nonlinear operator. By introducing the decomposition $\boldsymbol{q}(\boldsymbol{x}, t) = \boldsymbol{q}_0(\boldsymbol{x}, t) + \epsilon\, \boldsymbol{q}'(\boldsymbol{x}, t)$, with $\epsilon \ll 1$, the first-order dynamics are formulated as a linear

initial-value problem for the perturbation field,

$$\frac{\partial \boldsymbol{q}'}{\partial t} = \mathcal{L}(\boldsymbol{q}_0(\boldsymbol{x}, t))\, \boldsymbol{q}', \qquad \boldsymbol{q}'(\boldsymbol{x}, 0) = \boldsymbol{q}'_0, \tag{2}$$

where $\mathcal{L}(t, \boldsymbol{x})$ is the linearized operator obtained by matching orders of magnitude.

A key distinction from classical linear stability analysis is that the base state $\mathbf{q}_0$ is not time independent. The approach adopted in this work to develop the statistical framework assumes the quasi-steady-state approximation (QSSA), in which the base state is assumed frozen at each time instant and the linear operator is treated as time-independent. In particular, in this work, only the initial time $t_0 = 0$ is considered, for which an initial diffusive layer thickness is chosen. This simplification affects the predicted dynamics by considering an underlying separation of scales between the instability's evolution and the growth of the base state, as discussed by Ref. [17]. While the authors are actively working to extend the same statistical framework to time-dependent linear operators, such developments are beyond the scope of this study and will be discussed briefly. Consequently, the base state will be considered frozen at a specific time instant t_0, which acts as a parameter in the linear operator, i.e.,

$$\mathcal{L}(\boldsymbol{q}_0(\boldsymbol{x}, t_0)) = \mathcal{L}(t_0, \boldsymbol{x}). \tag{3}$$

Under this assumption, the trajectory of the linear initial-value problem can be expressed through the exponential propagator as

$$\boldsymbol{q}(t) = \exp(\mathcal{L}(\boldsymbol{x}, t_0)\, t)\ \boldsymbol{q}_0 = \mathcal{M}(t, t_0)\, \boldsymbol{q}_0, \tag{4}$$

where $\mathcal{M}(t, t_0)$ denotes the evolution operator. Unless stated otherwise, it is assumed that the linearized operator is homogeneous in the in-plane directions x and y, and that a suitable discretization is introduced for the non-homogeneous direction. The perturbation field is thus represented as a column vector $\mathbf{q}(t) \in \mathbb{C}^N$, and the linear operator as a matrix $\mathbf{L}(k_x, k_y, t_0) \in \mathbb{C}^{N\times N}$. The corresponding propagator is then expressed as the matrix exponential $\mathbf{M}(k_x, k_y, t) = \exp(\mathbf{L}\, t)$. The instantaneous perturbation energy is defined using a suitable inner product induced by the weight matrix $\mathbf{W} \in \mathbb{C}^{N\times N}$ as

$$e(t) = \|\mathbf{q}(t)\|_W^2 = \mathbf{q}(t)^*\, \mathbf{W}\, \mathbf{q}(t) = \mathrm{Tr}(\mathbf{q}(t)\, \mathbf{W}\, \mathbf{q}(t)^*)\,. \tag{5}$$

The *mean energy growth* is then introduced as the ratio between the mean energy at time t and its mean initial value,

$$G^{\mathrm{mean}}(t) = \frac{\mathbb{E}(e(t))}{\mathbb{E}(e(0))} = \frac{\mathrm{Tr}(\mathbf{M}\, \mathbf{C}_{00}\, \mathbf{M}^*\, \mathbf{W})}{\mathrm{Tr}(\mathbf{C}_{00}\, \mathbf{W})}, \tag{6}$$

where $\mathbf{C}_{00} = \mathbb{E}(\mathbf{q}_0\, \mathbf{q}_0^*)$ denotes the initial covariance of the perturbation field.

In this work, the emphasis is on the three-dimensional evolution of the mean energy growth, and the Wiener–Khinchin theorem is employed to express it as in Ref. [1]. In particular, it can be assumed without loss of generality, as will be shown later in this work, that the initial correlation is separable in the in-plane and vertical directions and that the in-plane statistics are homogeneous, namely, using the Hadamard product

$$\boldsymbol{C}_{00}(\boldsymbol{x}, \boldsymbol{x}') = \boldsymbol{C}_{00}^{xy}(x - x', y - y')\ \circ\ \boldsymbol{C}_{00}^{z}(z, z'). \tag{7}$$

Additionally, it is assumed that the in-plane homogeneous correlation is identical for all continuous variables. Under this assumption, the in-plane correlation no longer forms a matrix of continuous correlations; instead, it reduces to a single continuous function,

$$\boldsymbol{C}_{00}(\boldsymbol{x}, \boldsymbol{x}') = C_{00}^{xy}(x - x', y - y')\, \boldsymbol{C}_{00}^{z}(z, z'). \tag{8}$$

Letting $r_x = x - x'$ and $r_y = y - y'$, the two-dimensional Fourier transform of the initial correlation becomes

$$\widetilde{C}_{00}(k_x, k_y) = \iint C_{00}^{xy}(r_x, r_y)\, e^{-i(k_x r_x + k_y r_y)}\, dr_x\, dr_y \tag{9}$$

and the three-dimensional mean energy evolution is

$$G^{\mathrm{mean}}(t) = \frac{\displaystyle\iint g(k_x, k_y, t)\, \widetilde{C}_{00}(k_x, k_y)\, dk_x\, dk_y}{\mathrm{Tr}(\boldsymbol{C}_{00}^{z}) \displaystyle\iint \widetilde{C}_{00}(k_x, k_y)\, dk_x\, dk_y} \tag{10}$$

where

$$g(k_x, k_y, t) = \mathrm{Tr}\left(\mathbf{M}\,\mathbf{C}_{00}^{z}\,\mathbf{M}^{*}\right). \tag{11}$$

As will be discussed in Section IV.A, only the vertical velocity and density serve as variables governing the dynamics of the perturbations. Therefore, the state vector is defined as $\boldsymbol{q}(\boldsymbol{x}, t) = [w, \rho]^T$. Consequently, the correlation of the initial perturbations is given by

$$\mathbf{C}_{00}^{z}(z, z') = \begin{bmatrix} C_{00}^{z,ww}(z, z') & C_{00}^{z,w\rho}(z, z') \\ C_{00}^{z,\rho w}(z, z') & C_{00}^{z,\rho\rho}(z, z') \end{bmatrix}. \tag{12}$$

Throughout this analysis, all initial perturbations are assumed to originate from the density, a choice consistent with nearly all Rayleigh–Taylor studies and for which the only nonzero term in Eq.(12) is $C_{00}^{z,\rho\rho}(z, z')$ denoted, from now and on, as C_{00}^{z}.

III. Statistics of the initial perturbations

As demonstrated in Section IV.A, the self-similar evolution of the base state for the Rayleigh–Taylor instability can be expressed as

$$\rho(z, t) = 1 + \mathrm{At}\ \mathrm{erf}\left(\frac{z}{\delta_0}\right). \tag{13}$$

Given an initial time t_0, the initial perturbation is represented as a small interface displacement $\eta(x, y)$ such that $|\eta|/\delta_0 \ll 1$. The perturbed density can therefore be expressed as

$$\rho(\boldsymbol{x}) = \rho(z - \eta(x, y)) = 1 + \mathrm{At}\ \mathrm{erf}\left(\frac{z}{\delta_0}\right) - \frac{2\,\mathrm{At}}{\sqrt{\pi}\,\delta_0}\ \exp\left[-\left(\frac{z}{\delta_0}\right)^2\right] \eta(x, y) + O\left(\frac{\eta^2}{\delta_0^2}\right). \tag{14}$$

Assuming, without loss of generality, that $\eta(x, y)$ has zero mean

$$\mathbb{E}[\rho] = 1 + \mathrm{At}\ \mathrm{erf}\left(\frac{z}{\delta_0}\right), \tag{15}$$

the fluctuating component is

$$\rho' = \rho - \mathbb{E}[\rho] = -\frac{2\,\mathrm{At}}{\sqrt{\pi}\,\delta_0}\, e^{-(z/\delta_0)^2}\, \eta(x, y), \tag{16}$$

and eventually the correlation of the initial perturbations is

$$\boldsymbol{C}_{00}(\boldsymbol{x}, \boldsymbol{x}') = \frac{4\,\mathrm{At}^2}{\pi\,\delta_0^2}\ \exp\left(-\frac{z^2 + z'^2}{\delta_0^2}\right) \mathbb{E}[\eta(x, y)\,\eta(x', y')]\,. \tag{17}$$

This analysis leads to two main observations. First, for a self-similar profile, the initial profile is equivalent, to first order, to the average profile obtained by considering all possible (small) random perturbations of the interface. In this sense, the classical stability analysis around a diffusive interface can be interpreted as the evolution of the perturbation around the mean base state of all possible base states obtained by random perturbations of the interface, suggesting that the analysis of this problem must follow a statistical approach. Second, as discussed in the previous section, the initial correlation of disturbances in the Rayleigh–Taylor instability can be decomposed into a vertical non-homogeneous component and an in-plane component. The resulting correlation implies that the statistics of the perturbations in the vertical direction remain correlated over a distance comparable to the thickness of the diffusive layer. A larger value of δ corresponds to a smoother interface with slower vertical decorrelation, while a smaller δ produces a sharper interface and more rapid loss of vertical correlation. For the in-plane perturbation statistics an arbitrary modeling choice must be introduced. In this work, two types of in-plane correlations are considered, each representing a different modeling approach. The first is a Gaussian correlation, as proposed by Ref. [1], namely

$$C_{00}^{xy}(x - x', y - y') = \mathbb{E}[\eta(x, y)\,\eta(x', y')] \propto \exp\left[-\frac{(x - x')^2 + (y - y')^2}{\lambda^2}\right], \tag{18}$$

where λ denotes the correlation length of the initial disturbances. The second type of initial correlation is not assumed directly. Instead, it is derived from a common initialization method in direct numerical simulations that examine the

effects of initial perturbations, as in the works of Ref. [11, 18, 19], where, being L_x and L_y the dimensions of their numerical domains, the interface is modeled as a random linear combination of Fourier modes,

$$\eta(x,y) = \sum_p \sum_q A_{pq} \cos\!\left(\tfrac{2\pi}{L_x} p\, x + \psi_{pq}\right) \cos\!\left(\tfrac{2\pi}{L_y} q\, y + \phi_{pq}\right), \tag{19}$$

where the phases ψ_{pq} and ϕ_{pq} are independently drawn from the uniform distribution and the amplitudes A_{pq} are independent random variables with zero mean, specifically

$$\langle A_{k,m} A_{p,q} \rangle = \langle A_{k,m}^2 \rangle\, \delta_{k,p}\, \delta_{m,q}. \tag{20}$$

Under these assumptions, the corresponding correlation is computed directly from the ensemble of realizations of $\eta(x,y)$,

$$\begin{aligned}\mathbb{E}[\eta(x,y)\,\eta(x',y')] = \mathbb{E}\Big[\sum_{k,m} \sum_{p,q} A_{pq} A_{km} \cos\!\left(\tfrac{2\pi}{L_x} k\, x + \psi_{km}\right) \cos\!\left(\tfrac{2\pi}{L_y} m\, y + \phi_{km}\right) \\ \times \cos\!\left(\tfrac{2\pi}{L_x} p\, x' + \psi_{pq}\right) \cos\!\left(\tfrac{2\pi}{L_y} q\, y' + \phi_{pq}\right) \Big].\end{aligned} \tag{21}$$

Due to linearity and the independence of each phase, only terms with $k = p$ and $m = q$ contribute. Applying standard trigonometric identities yields

$$C_{00}^{xy}(x - x', y - y') = \sum_{p,q} \langle A_{p,q}^2 \rangle \cos\!\left(\tfrac{2\pi}{L_x}(x - x')p\right) \cos\!\left(\tfrac{2\pi}{L_y}(y - y')q\right). \tag{22}$$

Here, $\langle A_{p,q}^2 \rangle$ represents the energy allocated to each mode and defines the amplitude spectrum. The only statistical quantity influencing the evolution of the mean energy is the spectral content of the perturbation amplitudes, specifically the root-mean-square of the interface displacement. This is generally defined as the spectrum of the initial perturbation and constitutes a modeling choice. Henceforth, the energy spectrum is denoted as

$$S(k_{xp}, k_{yq}) = \langle A_{p,q}^2 \rangle, \qquad k_{xp} = \frac{2\pi p}{L_x}, \quad k_{yq} = \frac{2\pi q}{L_y}. \tag{23}$$

IV. Governing equations

This section analyzes two sets of governing equations for the Rayleigh–Taylor instability: the incompressible variable-density formulation and the Boussinesq approximation. The incompressible variable-density formulation for a binary mixing flow is presented first, followed by the Boussinesq approximation, which represents the limiting case for small density differences between the two fluids.

A. Incompressible variable-density formulation

Consider two miscible fluids arranged vertically under constant gravitational acceleration. The upper fluid is referred to as fluid 1 and the lower as fluid 2, with respective densities ρ_1 and ρ_2, and viscosities μ_1 and μ_2. The governing equations are the incompressible variable-density equations introduced by Ref. [16]. These equations are nondimensionalized using the reference quantities

$$\mu_r = \frac{\mu_1 + \mu_2}{2}, \quad \rho_r = \frac{\rho_1 + \rho_2}{2}. \tag{24}$$

These definitions yield a nondimensional system in which the Reynolds, Schmidt, Froude, and Atwood numbers are given by $\mathrm{Re} = \rho_r U_r L_r / \mu_r$, $\mathrm{Sc} = \mu_r/(\rho_r D)$, $\mathrm{Fr} = U_r/\sqrt{g L_r}$, and $\mathrm{At} = (\rho_1 - \rho_2)/(\rho_1 + \rho_2)$, and the resulting nondimensional governing equations read as

$$\begin{cases} \dfrac{\partial \rho}{\partial t} + \dfrac{\partial (\rho u_j)}{\partial x_j} = 0, \\ \rho \dfrac{\partial u_i}{\partial t} + \rho\, u_j \dfrac{\partial u_i}{\partial x_j} = -\dfrac{\partial p}{\partial x_i} + \dfrac{1}{\mathrm{Re}} \dfrac{\partial \tau_{ij}}{\partial x_j} + \dfrac{\rho\, g_i}{\mathrm{Fr}^2}, \\ \dfrac{\partial \log(\rho)}{\partial t} + u_j \dfrac{\partial \log(\rho)}{\partial x_j} = \dfrac{1}{\mathrm{Sc\,Re}} \nabla^2(\log(\rho)). \end{cases} \tag{25}$$

Here, $\tau_{ij} = 2\,\mu\,S_{ij} + \frac{4}{3}\,\mu\,\frac{\partial u_k}{\partial x_k}$, where $S_{ij} = \frac{1}{2}\left(\frac{\partial u_i}{\partial x_j} + \frac{\partial u_j}{\partial x_i}\right)$. Although the flow is incompressible, it is not divergence-free because of mixing effects. In particular, the divergence is constrained by

$$\frac{\partial u_i}{\partial x_i} = -\frac{1}{\mathrm{Sc\,Re}}\,\nabla^2(\log(\rho)). \tag{26}$$

Unless otherwise specified, Re = 1 and Fr = 1 are assumed, which fixes the velocity and length scales in the absence of intrinsic scales in the base flow. The lack of characteristic scales implies that the base flow exhibits self-similar evolution depending on a similarity variable that combines both z and t, as noted by Ref. [20]. By introducing the expansion $\mathbf{q}(\mathbf{x},t) = \mathbf{q}_0(z,t) + \epsilon\,\mathbf{q}'(\mathbf{x},t)$ and substituting into Eq.(25), the zeroth-order set of equations allows to express the evolution of the base state

$$\rho_0 = 1 + \mathrm{At}\,\mathrm{erf}\left(\frac{z}{\delta(t)}\right), \qquad \delta = \sqrt{\frac{4t}{\mathrm{Sc\,Re}}}. \tag{27}$$

Since the dilatational component introduces only a vertical velocity, no shear component is expected to couple the in-plane velocities with buoyancy and vertical motion. Therefore, the system of linearized equations can be reduced to a vertical velocity–density formulation. The procedure to obtain these equations involves deriving the Poisson equation, differentiating it with respect to z, and subsequently combining the result with the Laplacian of the vertical momentum equation. This approach eliminates the pressure term, yielding the reduced formulation and demonstrating that no coupling occurs between other components. A detailed derivation of the results obtained here, as well as the final functional expression for the linearized system, is reported in Appendix A, and the linearized system used is just reported compactly as

$$\begin{bmatrix} \mathcal{M}_{ww} & \mathcal{M}_{w\rho} \\ 0 & 1 \end{bmatrix} \begin{bmatrix} \frac{\partial w}{\partial t} \\ \frac{\partial \rho}{\partial t} \end{bmatrix} = \begin{bmatrix} \mathcal{L}_{w_0 w} + \mathcal{L}_{ww} & \mathcal{L}_{w_0\rho} + \mathcal{L}_{w\rho} \\ -\frac{\partial \rho_0}{\partial z} & \mathcal{L}_{\rho\rho} \end{bmatrix} \begin{bmatrix} w \\ \rho \end{bmatrix}. \tag{28}$$

After applying a Fourier transform in the homogeneous (x,y) directions and defining $k^2 = k_x^2 + k_y^2$, the system is discretized in the vertical direction and reformulated by introducing the state vector

$$\mathbf{q}_k(t) = \begin{bmatrix} \mathbf{w}_k(t) \\ \boldsymbol{\rho}_k(t) \end{bmatrix} \in \mathbb{C}^{2N_z} \tag{29}$$

to obtain the semi-discrete system

$$\mathbf{B}_k\,\frac{d\mathbf{q}_k}{dt} = \mathbf{A}_k\,\mathbf{q}_k \tag{30}$$

where the block matrices $\mathbf{A}_k$ and $\mathbf{B}_k$ follow from the discretization of Eq.(28) as

$$\mathbf{B}_k = \begin{bmatrix} \mathbf{M}_{ww} & \mathbf{M}_{w\rho} \\ \mathbf{0} & \mathbf{I} \end{bmatrix}, \qquad \mathbf{A}_k = \begin{bmatrix} \mathbf{L}_{w_0 w} + \mathbf{L}_{ww} & \mathbf{L}_{w_0\rho} + \mathbf{L}_{w\rho} \\ -\mathbf{D}_z\boldsymbol{\rho}_0 & \mathbf{L}_{\rho\rho} \end{bmatrix}, \tag{31}$$

where $\mathbf{D}_z$ is the discrete first derivative in z, and $\mathbf{I}$ is the identity matrix.

B. Boussinesq approximation

Although the Boussinesq equations for miscible flows are presented separately in this section, they are a direct consequence of the incompressible variable-density formulation, as demonstrated by Ref. [21]. More generally, these equations can be derived from the fully compressible Navier–Stokes equations for a binary mixture, as discussed by Ref. [22]. Upon nondimensionalization using the reference quantities defined in Eq.(24), the governing equations are given by

$$\begin{cases} \dfrac{\partial \boldsymbol{u}}{\partial t} + (\boldsymbol{u}\cdot\nabla)\boldsymbol{u} = -\nabla p + \dfrac{1}{\mathrm{Re}}\,\nabla^2\boldsymbol{u} - 2\mathrm{At}\,c\,\boldsymbol{e}_3, \\ \nabla\cdot\boldsymbol{u} = 0, \\ \dfrac{\partial c}{\partial t} + \boldsymbol{u}\cdot\nabla c = \dfrac{1}{\mathrm{Sc\,Re}}\,\nabla^2 c. \end{cases} \tag{32}$$

The same approach used to derive the evolution of the base state for the variable density formulation can be applied to the Boussinesq model. The sole distinction is that in the limit of small density differences, the flow field is divergence-free and the velocity base state can be decoupled from the concentration of species. Specifically, the base states are defined as $\boldsymbol{u}_0 = 0$ and $c_0(z) = \mathrm{erf}(z/\delta)$, where δ represents the width of the initial mixing layer. Employing the same methodology as in the derivation of the vertical velocity–density formulation in Appendix A, the linearized equations read,

$$\begin{cases} \dfrac{\partial \hat{w}}{\partial t} = \dfrac{1}{\mathrm{Re}}\left(\dfrac{\partial^2}{\partial z^2} - k^2\right)\hat{w} - 2\mathrm{At}\,k^2\left(\dfrac{\partial^2}{\partial z^2} - k^2\right)^{-1}\hat{c}, \\ \dfrac{\partial \hat{c}}{\partial t} = -\dfrac{\partial c_0}{\partial z}\,\hat{w} + \dfrac{1}{\mathrm{Sc\,Re}}\left(\dfrac{\partial^2}{\partial z^2} - k^2\right)\hat{c}. \end{cases} \tag{33}$$

The Fourier-transformed variables are $\hat{w}(k,z)$ and $\hat{c}(k,z)$ and by defining the state vector $\boldsymbol{q} = [\hat{w}, \hat{c}]^\mathsf{T}$, the governing equations can be written as

$$\frac{d}{dt}\begin{bmatrix}\hat{w}\\ \hat{c}\end{bmatrix} = \begin{bmatrix} \dfrac{1}{\mathrm{Re}}\left(\dfrac{\partial^2}{\partial z^2} - k^2\right) & -2\mathrm{At}\,k^2\left(\dfrac{\partial^2}{\partial z^2} - k^2\right)^{-1} \\ -\dfrac{\partial c_0}{\partial z} & \dfrac{1}{\mathrm{Sc\,Re}}\left(\dfrac{\partial^2}{\partial z^2} - k^2\right) \end{bmatrix}\begin{bmatrix}\hat{w}\\ \hat{c}\end{bmatrix}, \tag{34}$$

whose compact form is

$$\frac{d\boldsymbol{q}}{dt} = \boldsymbol{A}(k,z)\,\boldsymbol{q}. \tag{35}$$

V. Numerical solver

Following the derivation of the governing equations, a solver employing a Chebyshev spectral method is developed using the MATLAB differentiation suite of Ref. [23]. To resolve the sharp gradient of the initial profile, a coordinate transformation that concentrates collocation points within the diffusive layer is introduced. For a physical domain $[a,b] = [-L_z, L_z]$, the mapping is

$$z(\xi) = \frac{a+b}{2} + \frac{b-a}{2}\,\frac{\sinh(\alpha\,\xi)}{\sinh(\alpha)}, \quad \xi \in [-1,1],\ z \in [a,b], \tag{36}$$

where the free parameter α controls the clustering: for $\alpha \gg 1$ most points fall near $z = 0$. The inverse mapping, required to construct the spectral matrices, follows from

$$\frac{dz}{d\xi} = \frac{b-a}{2}\,\frac{\alpha\,\cosh(\alpha\,\xi)}{\sinh(\alpha)}, \qquad \frac{d\xi}{dz} = \left(\frac{dz}{d\xi}\right)^{-1} = \frac{2}{b-a}\,\frac{\sinh(\alpha)}{\alpha\,\cosh(\alpha\,\xi)}. \tag{37}$$

Hence, the first-derivative matrix in physical space requires only the Chebyshev matrix $D^{(\xi)}$

$$\left.\frac{df}{dz}\right|_{z_i} \approx \sum_{j=1}^{N} \underbrace{\left(\frac{dz}{d\xi}\right)_{\xi_i}^{-1}}_{w_i} D_{ij}^{(\xi)}\,f_j, \qquad D^{(z)} = \mathrm{diag}(w_i)\,D^{(\xi)}. \tag{38}$$

For the second derivative,

$$\frac{d^2 f}{dz^2} = \left(\frac{d\xi}{dz}\right)^2\frac{d^2 f}{d\xi^2} + \frac{d^2\xi}{dz^2}\frac{df}{d\xi}, \qquad \frac{d^2\xi}{dz^2} = -\frac{d^2 z}{d\xi^2}\left(\frac{dz}{d\xi}\right)^{-3}, \tag{39}$$

so that

$$\left(D^{(z,2)}\mathbf{f}\right)_i \approx w_i^2\left(D^{(\xi,2)}\mathbf{f}\right)_i + u_i\left(D^{(\xi,1)}\mathbf{f}\right)_i, \qquad w_i = \left.\frac{d\xi}{dz}\right|_{z_i},\ u_i = \left.\frac{d^2\xi}{dz^2}\right|_{z_i}, \tag{40}$$

and eventually

$$D^{(z,2)} = \mathrm{diag}\left(w_i^2\right)D^{(\xi,2)} + \mathrm{diag}\left(u_i\right)D^{(\xi,1)}. \tag{41}$$

Because the main quantity of interest is an energy functional defined through an integral, we must introduce a weight matrix concerning the integration rule employed. The classical Clenshaw–Curtis rule gives

$$W_\xi = \mathrm{diag}(\eta_i \left.\frac{dz}{d\xi}\right|_i), \tag{42}$$

where the η_i are the standard Clenshaw–Curtis weights as reported in Ref. [24].

VI. Energy of the disturbances

The notion of disturbance energy, first introduced in Section IV.A through Eq.(5), deserves a more detailed discussion, which is the focus of this section. The challenge of properly defining the energy associated with a disturbance in a flow field traces back to the work of Ref. [25], who established two fundamental requirements: the disturbance energy must (i) be a positive-definite quantity with the physical dimensions of energy, and (ii) decay monotonically in time in the absence of external forcing. These criteria lead to the classical energy norm for linearized disturbances in fluid flows, a formulation that, despite its age, continues to be used in modern studies such as Ref. [26, 27]. Subsequent developments extended this framework beyond linear approximations. Ref. [28] introduced an exact *energy corollary* valid for arbitrary disturbances in steady viscous flows, which naturally reduces to the linear form when linearized perturbations remain accurate predictors of disturbance evolution. Later, Ref. [29] generalized this formulation to reactive and combusting flows by incorporating the effects of species transport and heat release. For the present analysis of the Rayleigh–Taylor instability, one may adapt this theoretical framework by relaxing the vanishing-body-force constraint. Following an approach similar to Ref. [30], and requiring that the buoyancy production term balances the vertical transport of the mean density, the following expression for the evolution of the disturbance energy can be obtained for a Boussinesq flow,

$$\frac{dE}{dt} = \frac{d}{dt}\int_V \left(\frac{u_i u_i}{2} - \frac{2\,\mathrm{At}}{\rho_{0,z}}\frac{\rho^2}{2}\right) dV = -\frac{1}{\mathrm{Re}}\int_V \frac{\partial u_i}{\partial x_j}\frac{\partial u_i}{\partial x_j}\,dV + 2\,\mathrm{At}\int_V \frac{1}{\rho_{0,z}}\frac{\partial \rho}{\partial x_j}\frac{\partial \rho}{\partial x_j}\,dV. \tag{43}$$

In this formulation, the Brunt–Väisälä frequency naturally appears as a weighting factor in the quadratic form of the density perturbation. However, the resulting expression is positive definite and nonincreasing in time only when $\rho_{0,z} < 0$, indicating that the flow must be stably stratified for a proper energy norm to exist. One might argue that relaxing the assumption of the absence of external body forces could yield an incorrect definition of energy. Still, this limitation is not unique to the present derivation. Indeed, Ref. [31] obtained an analogous expression—through a different reasoning—where the energy norm remains positive definite solely for a stably stratified base state. Consistent findings from subsequent works [32–34] further support that no quadratic, positive-definite energy norm can be formulated for an unstably stratified flow. A possible way to circumvent the positive-definiteness issue is to adopt the approach of Ref. [17], in which the energy associated with the concentration field is simply defined as a quadratic quantity. While such formulations offer a convenient means of evaluating perturbation growth, they do not resolve the fundamental problem that these definitions are dimensionally inconsistent (unless properly nondimensionalized) and therefore do not represent a true physical energy. Furthermore, as noted by the same authors, the resulting measures are sensitive to the specific terms included in the definition, introducing ambiguity in identifying the quantity that genuinely governs transient dynamics. Recognizing the practical difficulty of defining a positive-definite norm that emerges naturally from the governing conservation equations, we pursue a different strategy. Rather than adopting an arbitrary definition and testing its sensitivity, the objective is to establish an energy norm still grounded in the conservation principles, one that, in the limit of a stably stratified flow, recovers the physically meaningful available potential energy described by Ref. [32]. The formulation proposed here builds on the framework of available potential energy developed by Ref. [34], and the subsequent derivation will closely follow their theoretical treatment.

Before proceeding, it is necessary to introduce, at least qualitatively, the notion of a *reference state*. Following the definition of Ref. [33], the reference state corresponds to the adiabatic rearrangement of the initial base density field such that the gravitational potential energy is minimized. Indeed, for the potential energy to be defined, a reference state must be specified. Since this choice is, in principle, arbitrary, it is natural to select the configuration that minimizes the potential energy and this will be referred to as the *reference profile*.

The first step is to note that the reference state, obtained through the adiabatic rearrangement of the initial density profile, coincides with the inverted version of the initial profile of a classical unstable diffusive error-function stratification. For simplicity, only a diffusive error-function profile is considered here, although the same reasoning applies to any

monotonically increasing profile in the vertical direction. Let be H the Heaviside step function

$$H\big(\rho(\mathbf{x},t)-\rho(\mathbf{x}_0,t)\big)=\begin{cases}0, & \rho(\mathbf{x},t)<\rho(\mathbf{x}_0,t),\\ \frac{1}{2}, & \rho(\mathbf{x},t)=\rho(\mathbf{x}_0,t),\\ 1, & \rho(\mathbf{x},t)>\rho(\mathbf{x}_0,t)\end{cases} \tag{44}$$

for which, following Ref. [34]

$$V(\rho)=\frac{1}{V_r}\int_{\rho(z)<\rho} dV=\frac{1}{V_r}\int_{V_r} H(\rho(z)-\rho)\,dV \tag{45}$$

represent the fraction of the total volume whose density is lower than ρ. In the case where $\rho=\rho(z)$, this can be interpreted as the fraction of the vertical domain whose density is below ρ, that is,

$$V(\rho)=\frac{1}{L_z}\int H(\rho(z)-\rho)\,dz. \tag{46}$$

For a monotonically increasing profile, denoting by $z(\rho)$ the inverse of the initial unstable profile, we obtain

$$V(\rho)=\frac{z(\rho)}{L_z}. \tag{47}$$

The sorted (or reference) profile, by definition, satisfies

$$z^*(\rho)=z(V(\rho)). \tag{48}$$

Differentiating this last expression

$$\frac{\partial z^*}{\partial\rho}=\frac{\partial z}{\partial V}\frac{\partial V}{\partial\rho}=-L_z\frac{\partial V}{\partial\rho}=\frac{\delta\sqrt{\pi}}{2\,\mathrm{At}}\exp\left(\frac{z^2}{\delta^2}\right)=\left(\frac{\partial\rho_r}{\partial z}\right)^{-1} \tag{49}$$

it follows that the reference (sorted) density profile can be expressed as

$$\rho_r(z)=1+\mathrm{At}\,\mathrm{erf}\left(-\frac{z}{\delta}\right), \tag{50}$$

which corresponds exactly to the stably stratified counterpart of the initial unstable profile.

Having identified the background sorted profile, we now aim to measure perturbation energies relative to this stable reference state. However, it is not immediately evident that perturbations about the unstable Rayleigh–Taylor profile are equivalent to those about the stable, sorted profile. It is therefore necessary to establish a relationship between the two. Let $z^*(z)$ denote the sorting function, defined such that $\rho_r(z^*(z))=\rho_0(z)$. Consider a fluid parcel labeled a, with density ρ_a, satisfying $\rho_r(z^*(z_a))=\rho_0(z_a)=\rho_a$. A small vertical displacement of this parcel in the two profiles can then be expressed, following Ref. [31], as

$$\rho_r(z^*-\eta_*)=\rho_r(z_a^*)+\left.\frac{\partial\rho_r}{\partial z^*}\right|_a\eta_*\Rightarrow\rho_r'=\rho_r-\rho_a=-\left.\frac{\partial\rho_r}{\partial z^*}\right|_a\eta_*, \tag{51}$$

$$\rho(z-\eta_0)=\rho(z_a)+\left.\frac{\partial\rho}{\partial z}\right|_a\eta_0\Rightarrow\rho'=\rho-\rho_a=-\left.\frac{\partial\rho}{\partial z}\right|_a\eta_0. \tag{52}$$

By showing that the stably stratified profile is simply the inverted version of the unstable one, it follows that the gradients of ρ_r and ρ are equal in magnitude but opposite in sign, namely,

$$\left.\frac{\partial\rho_r}{\partial z^*}\right|_a=-\left.\frac{\partial\rho}{\partial z}\right|_a. \tag{53}$$

Since $(\eta_*-\eta_0)$ is a small quantity, it can be concluded that

$$\rho_r'=-\rho'+O(\eta). \tag{54}$$

The disturbance energy can thus be written in the general form

$$E(k) = \int_{-L_z}^{L_z} \left(|\hat{u}|^2 + |\hat{v}|^2 + |\hat{w}|^2 \right) dz + \int_{-L_z}^{L_z} \frac{2\,\mathrm{At}}{\frac{\partial \rho_r}{\partial z}} \frac{|\hat{\rho}|^2}{2}\, dz. \tag{55}$$

Because the background stratification is modeled with an error-function profile, the Brunt–Väisälä frequency depends exponentially on z. As a result, it grows without bound outside the mixing layer. This behavior, however, is merely a byproduct of the analytical form of the erf profile. Physically, it reflects the fact that beyond the diffusive layer there is no stratification and hence no available potential energy [35]. It is therefore reasonable to assume that the contribution outside the diffusive layer is zero, leading to

$$E(k) = \int_{-L_z}^{L_z} \left(|\hat{w}|^2 + \frac{1}{k^2} \left| \frac{d\hat{w}}{dz} \right|^2 \right) dz + \int_{-\delta}^{\delta} \frac{\sqrt{\pi}\,\delta}{2} |\hat{\rho}|^2\, dz. \tag{56}$$

This derivation, as clarified at the beginning of this discussion, is not intended to overcome the fundamental limitation of defining a positive-definite quadratic energy norm, assuming such a definition even exists. Rather, it represents a mathematical construction that connects the notion of energy to a quantity that is at least dimensionally consistent with a physical energy and, in the case of a stably stratified flow, reduces to the available potential energy that carries a clear physical interpretation. At the present stage, no direct physical meaning can be ascribed to this construction beyond its dimensional consistency with an energy norm.

Since the present analysis will be extended to the variable-density case, it is necessary to determine whether the previous results remain valid. All previous studies defining the energy norm rely on the Boussinesq approximation, which raises the question of whether such definitions can be consistently extended to variable-density flows. Fortunately, this extension is relatively straightforward. Under adiabatic rearrangement of fluid particles—meaning no mixing—the variable-density formulation implies that the logarithm of the density is conserved. Because the logarithm is a monotonic function, sorting by density in logarithmic space is equivalent to sorting in physical space. Following Ref. [33], this can be written as

$$z_*(\mathbf{x}, t) = \frac{1}{A} \int_V H(\rho(\mathbf{x}', t) - \rho(\mathbf{x}, t))\, dV' = \frac{1}{A} \int_V H(\log \rho(\mathbf{x}', t) - \log \rho(\mathbf{x}, t))\, dV', \tag{57}$$

where variable $z^*(\mathbf{x}, t)$ represents a length that can be interpreted as a statically stable ordering of fluid elements [31]. To extend Eq.(43) to the variable-density case, it is necessary to derive an equivalent bilinear form, noting that the divergence-free constraint cannot be exploited in the presence of nonzero mixing. Consider the vertical vorticity equation for the linearized variable-density system,

$$\rho_0 \frac{\partial \zeta_3}{\partial t} = 2\mu' \frac{\partial \zeta_3}{\partial x_3} + \mu \nabla^2 \zeta_3. \tag{58}$$

This result implies that if the initial condition does not introduce vertical vorticity, the vertical vorticity remains zero during the evolution of the perturbation. Exploiting the divergence constraint for the variable-density formulation and using the fact that the in-plane vorticity remains zero during evolution, the system can be written as

$$\begin{aligned} i\,k_y \hat{u} - i\,k_z \hat{v} &= 0, \\ i\,k_x \hat{u} + i\,k_y \hat{v} &= \mathcal{L}_\rho^{\nabla^2}\, \hat{\rho} - \frac{\partial \hat{w}}{\partial z}. \end{aligned} \tag{59}$$

The total disturbance energy for the variable-density case can then be expressed as

$$E_{VD}(k) = \int_{-L_z}^{L_z} \left(|\hat{w}|^2 + \frac{1}{k^2} \left| \mathcal{L}_\rho^{\nabla^2}\, \hat{\rho} - \frac{\partial \hat{w}}{\partial z} \right|^2 \right) dz + \int_{-\delta}^{\delta} \frac{\delta\sqrt{\pi}}{2} |\hat{\rho}|^2\, dz. \tag{60}$$

VII. Statistical evolution of the mean energy

As discussed in Section III, the first type of in-plane correlation used to describe the interface perturbations is modeled by an isotropic Gaussian

$$C_{00}^{xy}(x - x', y - y') = \exp\left[-\frac{(x - x')^2 + (y - y')^2}{\lambda^2} \right]. \tag{61}$$

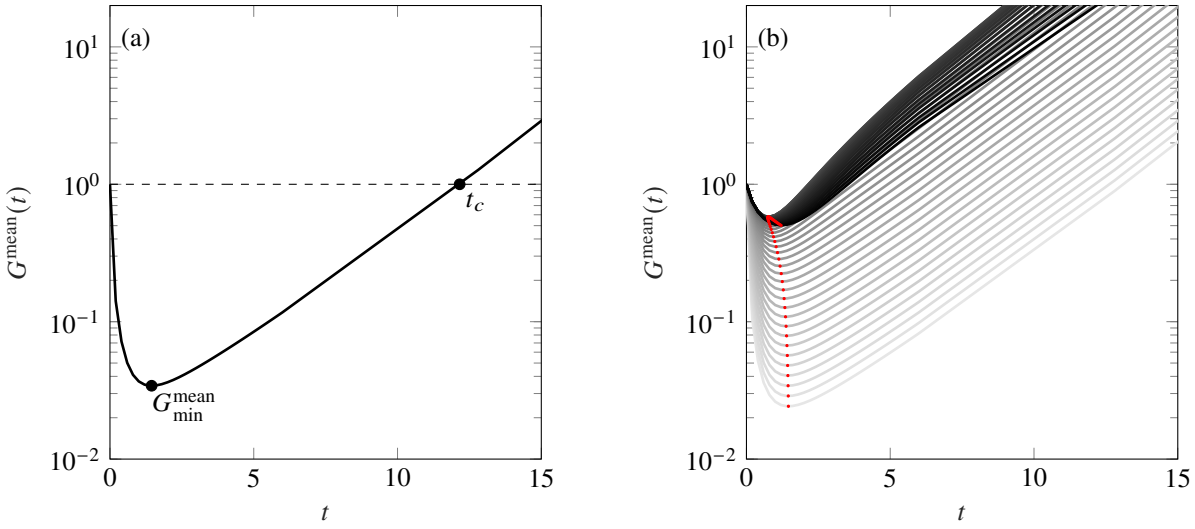

Fig. 1 Temporal evolution of $G^{\text{mean}}(t)$ at $A_t = 0.5$ within the Boussinesq approximation for different horizontal correlation lengths λ. (a) Single trajectory illustrating the characteristic quantities of interest in this study. (b) Evolution of multiple trajectories for various λ values, highlighting the non-monotonic dependence of the minimum energy attained during the evolution on the correlation length.

The parameter λ represents the horizontal correlation length in the (x, y)-plane, corresponding to the characteristic distance over which perturbations of the interface height remain statistically correlated. A small λ implies highly uncorrelated, white-noise–like perturbations, whereas a large λ produces coherent, long-wavelength undulations at the same physical scale. A Gaussian model for the in-plane statistics thus provides a compact yet physically meaningful representation of the surface roughness characterizing the initial perturbation of the interface.

For the Rayleigh–Taylor configuration the linearized equations depend only on the magnitude of the wavenumber. Switching to polar coordinates (k, θ) reduces the mean energy growth defined in Eq.(10) to

$$G^{\text{mean}}(t) = \left[g(0,t) + \int_0^\infty \frac{\partial g(t,k)}{\partial k} \exp\left(-\frac{\lambda^2 k^2}{4}\right) dk \right]. \tag{62}$$

Up to this point, the formulation has been general and applicable to both the variable-density and the Boussinesq cases. However, in this section, the results refer specifically to the linear operator derived under the Boussinesq approximation, as defined in Eq.(34). In Fig. 1a, a representative evolution of $G^{\text{mean}}(t)$ is shown for a fixed value of $\lambda = 0.6$. The mean energy initially decays nearly exponentially, reflecting the dominance of stable eigenmodes at early times. This decay continues until a minimum value, $G^{\text{mean}}_{\text{min}}(\lambda)$, is reached. Beyond this point, the trajectory reverses and exhibits exponential growth driven by the unstable modes present in the spectrum. A key feature of this behavior is the time delay observed in the divergence of the trajectories. To quantify this delay, the *critical time* t_c is defined as the instant, distinct from the initial one, at which $G^{\text{mean}}(t_c) = 1$. In this sense, it can be viewed as a time delay if the system diverges from the moment the initial perturbation is applied. In Fig. 1b, the temporal evolution of $G^{\text{mean}}(t)$ is shown for several values of the in-plane correlation length λ. Lighter curves correspond to smaller values of λ, whereas progressively darker tones indicate larger values. The ordering of the trajectories highlights the non-monotonic dependence of the minimum value attained during the evolution on the correlation length, which is reported in red for each trajectory. Since there is a direct functional relationship between the evolution of the mean energy growth and the initial correlation, it is possible to describe the physical mechanisms that lead to this non-monotonic behavior. In fact, the evolution of the mean energy is modulated by the exponential kernel in Eq.(62), which acts as a low-pass filter. As the correlation length λ increases from zero, large-k (stable) modes are progressively filtered out, causing the delay to decrease until a minimum is reached. Beyond this point, however, low-k (unstable) modes are also filtered out, leading to a subsequent increase in the time delay. In fact, for small λ, the kernel is nearly flat and all wavenumbers contribute, so the early-time dynamics are dominated by stable modes and the minimum $G^{\text{mean}}_{\text{min}}$ is correspondingly lower. As λ grows, the influence of stable modes diminishes and $G^{\text{mean}}_{\text{min}}$ increases; once λ becomes sufficiently large, the suppression of unstable modes causes $G^{\text{mean}}_{\text{min}}$ to decrease again. This behavior reflects a transient stabilization effect induced by small-scale roughness

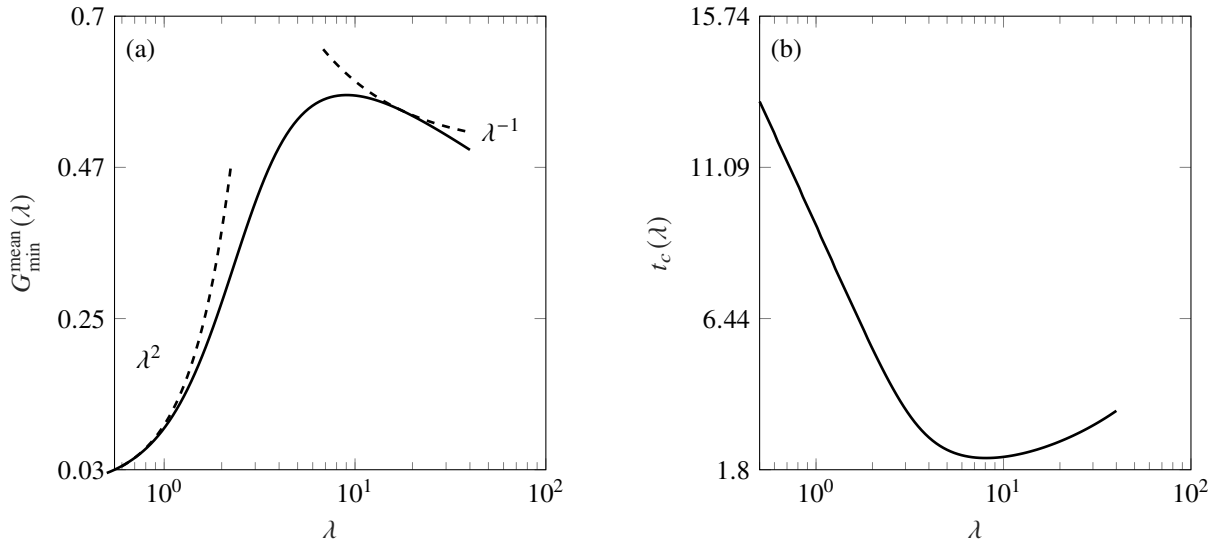

Fig. 2 Minimum values $G^{\text{mean}}_{\text{min}}$ and critical times t_c obtained within the Boussinesq approximation. (a) Dependence of $G^{\text{mean}}_{\text{min}}$ on λ and Atwood number. (b) Variation of the critical time t_c with λ for $A_t = 0.2$, emphasizing the non-monotonic behavior of both quantities with respect to the horizontal correlation length.

and highlights the sensitivity of the energy growth to the horizontal correlation length.

Additionally, to quantify the dependence of G^{mean} on the correlation length, asymptotic expansions of Eq.(62) can be derived. In the limit $\lambda \to \infty$,

$$G^{\text{mean}}(t) \approx \frac{1}{\text{Tr}\left(\boldsymbol{C}^z_{00}\right)} \left(g(t,0) + \left.\frac{\partial g}{\partial k}\right|_{(t,0)} \frac{\sqrt{\pi}}{\lambda} \right), \tag{63}$$

while for $\lambda \to 0$

$$G^{\text{mean}}(t) \approx \frac{\lambda^2}{2\ \text{Tr}\left(\boldsymbol{C}^z_{00}\right)} \int_0^\infty g(t,k)\, k\, dk. \tag{64}$$

The asymptotic behavior is illustrated in Fig. 2 for the minimum values attained during the transient evolution. The small-λ regime is consistent with the quadratic scaling predicted by Eq.(64), indicating that for very short correlation lengths the energy decreases by several orders of magnitude relative to its initial value and exhibits a clear quadratic dependence on λ. An intermediate regime follows, where the asymptotic dependence transitions to the λ^{-1} scaling. As λ increases further, however, this asymptotic behavior is lost. A possible explanation is that, for large λ, the Gaussian kernel approaches the Dirac-delta function, which may introduce inaccuracies in the numerical integration procedure used to compute this quantity.

After analyzing the mean energy growth under Gaussian perturbations, the focus is now shifted to the second modeling choice for the in-plane disturbances, namely the one associated with the initialization of direct numerical simulations. Within this framework, it is possible to derive a closed-form expression for the mean energy growth expected from a three-dimensional perturbation with a prescribed spectrum. In particular, by substituting the correlation in Eq.(22) into the general expression for the mean energy growth given in Eq.(10), the following closed-form expression is obtained,

$$G^{\text{mean}}(t) = \frac{\displaystyle\sum_{\kappa} S(\kappa)\ \text{Tr}\left\{\mathbf{M}_t(\kappa)\, \mathbf{C}^z_{00}\, \mathbf{M}^*_t(\kappa)\right\}}{\text{Tr}\left(\mathbf{C}^z_{00}\right) \displaystyle\sum_{\kappa} S(\kappa)}. \tag{65}$$

Two principal observations follow from Eq.(65). First, the only statistical quantity that influences the evolution of the mean energy is the spectral content of the perturbation amplitudes, specifically the root-mean-square of the interface displacement. Second, and more relevant from a practical standpoint, all computations involving the linear operator can

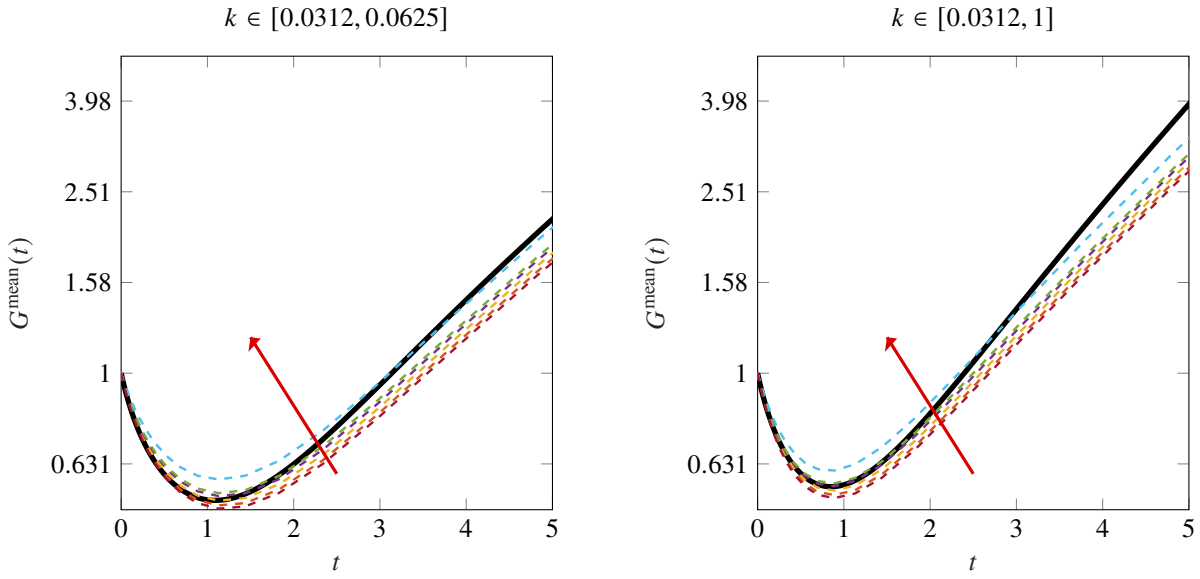

Fig. 3 Comparison between linear-stability predictions and the direct numerical simulations at Atwood number $A_t = 0.5$ with flat spectrum $S(k) = 1$ for the configurations in Table 1. The two cases correspond to increasing values of δ, highlighting the effect of initial diffusive-layer variations.

be performed *a priori* for each wavelength and stored offline. These precomputed results can then be weighted by any desired spectrum, eliminating the need to perform a new simulation for each spectral distribution.

CASE	N_x	N_y	N_z	L_x	L_y	L_z	N_{min}	N_{max}	E_0	k_{min}	k_{max}
1	64	64	512	64π	64π	16π	1	2	0.05	0.0312	0.0625
2	64	64	512	64π	64π	16π	1	32	0.05	0.0312	1

Table 1 Parameters employed in the numerical simulations for each case. All simulations were performed at Atwood number $A_t = 0.5$ with a flat initial spectrum $S(k) = 1$, meaning that all wavenumbers within the range $[k_{\text{min}}, k_{\text{max}}]$ are equally weighted. The quantities N_x, N_y, and N_z denote the number of grid points in the streamwise, spanwise, and vertical directions, respectively, while L_x, L_y, and L_z denote the corresponding domain dimensions. The parameters N_{min} and N_{max} indicate the lower and upper bounds on the number of Fourier modes included in the response. The wavenumber k_{min} represents the smallest wavenumber resolved by the computational domain, whereas $k_{\text{max}} = N_{\text{max}} k_{\text{min}}$ corresponds to the largest wavenumber included in the initial perturbation spectrum. The parameter E_0 denotes the initial perturbation energy level.

Since the initial perturbation follows the standard setup commonly used in direct numerical simulations to assess the influence of initial conditions, the predictions from the linear stability solver are compared against numerical data obtained for a flat spectrum $S(k) = 1$. These numerical results are produced using the triple-periodic pseudo-spectral code PsDNS (`https://github.com/lanl/PsDNS.git`) and the configurations used for the simulations are summarized in Table 1. For each case, five independent ensembles were generated, and their results were averaged to obtain the statistical mean energy growth, corresponding to an average normalized energy of 0.5. Fig. 3 shows close agreement between the linear solver and the numerical simulations at early times. For random initial conditions, a noticeable time delay in the evolution is observed, consistent with predictions from the statistical linear framework. Fig. 3 also displays several trajectories from the linear solver corresponding to different initial interface thicknesses in the range $\delta \in [1, 1.2]$, illustrating that thicker initial layers maintain improved agreement at later times. This behavior indicates that the base state is not stationary but instead thickens progressively due to diffusion. Consequently, assuming a fixed interface thickness in the linear solver introduces discrepancies relative to the numerical simulations, where the diffusive layer naturally broadens over time. This interpretation is further supported by trajectories associated with larger k_{max} in the random initial field, which include a greater contribution from stable (diffusive) modes. In these cases, the diffusive

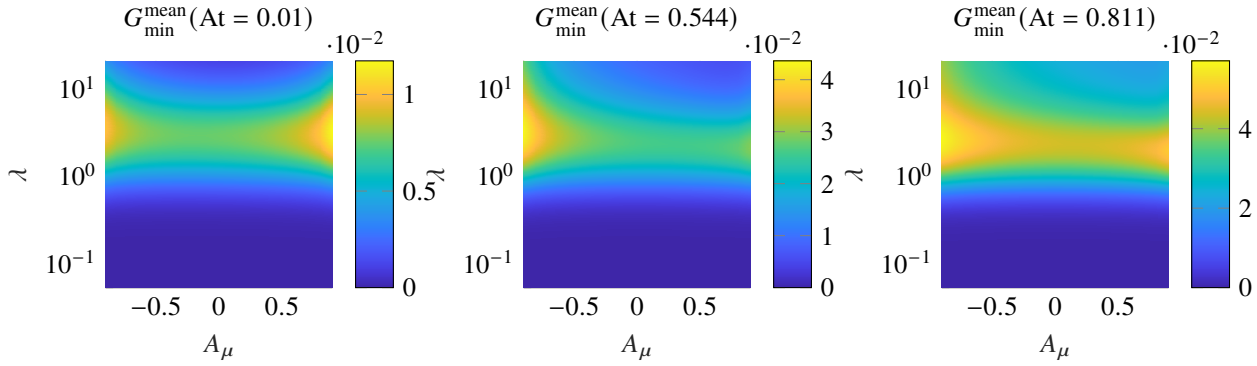

Fig. 4 Effect of density contrast on the minimum mean growth $G^{\text{mean}}_{\text{min}}$ for different viscosity ratios A_μ. For small Atwood numbers, viscosity effects are nearly symmetric; at higher Atwood numbers, negative A_μ (heavier fluid more viscous) reduces the delay time, leading to earlier instability growth.

layer grows more rapidly, leading to an earlier departure from the statistical linear predictions. Although part of the discrepancy may originate from statistical noise due to the limited ensemble size (five realizations), the differences between trajectories remain small during the non-monotonic phase. These observations reinforce the conclusion that the evolving diffusive layer significantly influences the statistical evolution of the mean energy, consistent with previous findings in Ref. [36].

VIII. Mean energy growth for Incompressible variable-density equations

The major limitation of the Boussinesq approximation is that it allows analysis of variable-density flows only in the limit of small density differences. This restriction is significant in practice, since, for example, the Atwood number for a mixture of air and helium is $\text{At} \approx 0.75$ [37]. Most studies on incompressible variable-density flows have focused on large-scale numerical simulations aimed at understanding the turbulent features of Rayleigh–Taylor mixing layers [12, 21, 38]. However, to the author's knowledge, no prior study has analyzed the incompressible variable-density equations in the context of linear stability, nor has any attempt been made to characterize them statistically. This step is pursued here and extends the previous work, aiming to characterize the effect of density differences, including viscosity stratification, and to report results from the variable-density model in Eq.(28) for a Gaussian in-plane correlation. The viscosity stratification is defined by an equivalent viscosity Atwood number

$$\text{A}_\mu = \frac{\mu_1 - \mu_2}{\mu_1 + \mu_2}, \tag{66}$$

for which the viscosity profile is modeled as

$$\mu(z) = 1 + \text{A}_\mu \,\text{erf}\left(\frac{z}{\delta_0}\right). \tag{67}$$

The analysis in this section focuses on the effect of density contrast on the minimum mean growth $G^{\text{mean}}_{\text{min}}$, which is directly related to the critical time t_c characterizing the onset of divergence in the statistical response. Therefore, the trajectory depth and the delay time are treated interchangeably in the discussion. The parameter space explored spans $\text{At} \in [0, 0.85]$ and $\text{A}_\mu \in [-0.9, 0.9]$. Fig. 4 shows results for $\text{At} = 0.01$ (small Atwood number), $\text{At} = 0.544$ (intermediate Atwood number), and $\text{At} = 0.811$ (large Atwood number). The first observation is that viscosity effects remain mild for $|\text{A}_\mu| \lesssim 0.9$, consistent with Ref. [39], which reported only slight variations due to viscosity in the RTI stability spectrum. Secondly, in regimes where viscosity stratification has a non-negligible effect, an increase in the trajectory depth, or equivalently, a reduction in the time delay, is observed. By fixing the viscosity contrast and analyzing the effect of the Atwood number, a strong asymmetry emerges depending on the sign of A_μ. For small Atwood numbers, the influence of viscosity is nearly symmetric, as expected in this limit from the Boussinesq approximation. In contrast, for larger Atwood numbers, a negative A_μ reduces the time delay, leading to an earlier divergence of the instability. This asymmetry persists at high Atwood numbers, where viscosity effects also become significant for intermediate values of A_μ. Fig. 5 presents the complementary perspective: for fixed values of A_μ, the variation of $G^{\text{mean}}_{\text{min}}$ with Atwood number

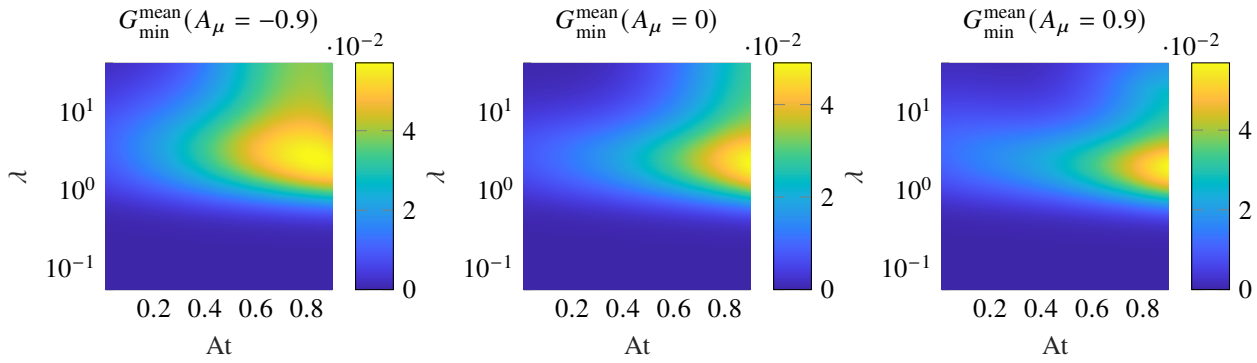

Fig. 5 Effect of viscosity contrast on $G^{\text{mean}}_{\text{min}}$ for different density contrasts At**. For** At ≥ 0**, the peak is located at the highest Atwood number computed. When** $A_\mu < 0$**, the minimum shifts toward smaller** At**, indicating an earlier onset of instability.**

is examined. When viscosity differences are absent ($A_\mu = 0$), $G^{\text{mean}}_{\text{min}}$ exhibits a peak at the largest density contrast, and a similar dependence on the Atwood number is observed for $A_\mu \approx 0.9$. Interestingly, for $A_\mu \approx -0.9$, the peak shifts toward At ≈ 0.8, indicating that the instability develops earlier in this configuration.

IX. Conclusion

This work employed and extended the statistical framework of Ref. [1] to analyze how different classes of initial perturbations influence the linear evolution of the Rayleigh–Taylor instability. The approach enabled closed-form expressions for the growth of the mean perturbation energy and provided a means to characterize the transient dynamics before instability amplification becomes dominant. For perturbations modeled with Gaussian in-plane correlations, the evolution of $G^{\text{mean}}(t)$ exhibits an initial decay followed by exponential growth. The transition between these regimes is marked by a critical time t_c, which was shown to depend non-monotonically on the correlation length λ. This demonstrates that multimodal perturbations may delay the onset of instability in a nontrivial way, with neither highly localized nor highly coherent disturbances producing the strongest or fastest-growing response. Instead, the dominant contribution results from a balance between stable and unstable spectral components that depends directly on λ. For perturbations defined as random superpositions of Fourier modes, an analytical expression for $G^{\text{mean}}(t)$ was derived in terms of the initial spectral amplitudes. This formulation clarifies the contribution of specific wavenumber bands and allows direct comparison with ensembles of three-dimensional DNS. The agreement observed during the linear stages confirms that the statistical framework provides predictive capability, while the deviations appearing at later times reflect the inherently non-autonomous character of the evolving base state. Finally, the effects of viscosity and density stratification were examined. Both modify the growth rate and shift the critical time, but do not eliminate the transient delay mechanism. These results highlight that the statistical structure of the initial perturbations plays a central role in shaping early-time RTI evolution and should be taken into account when designing or interpreting experiments and numerical simulations.

A. Derivation of the Velocity–Density Formulation

A detailed description and derivation of the set of equations briefly discussed in Section IV.A are reported here. By introducing the expansion $\boldsymbol{q}(\boldsymbol{x},t) = \boldsymbol{q}_0(z,t) + \epsilon\,\boldsymbol{q}'(\boldsymbol{x},t)$ and substituting into Eq.(25), the zeroth-order set of equations are given by

$$\frac{\partial \rho_0}{\partial t} + \frac{\partial(\rho_0 U_{j0})}{\partial x_j} = 0, \tag{68a}$$

$$\rho_0 \frac{\partial U_{i0}}{\partial t} + \rho_0 U_{j0} \frac{\partial U_{i0}}{\partial x_j} = -\frac{\partial p_0}{\partial x_i} + \frac{1}{Re}\frac{\partial \tau_{ij0}}{\partial x_j} + \rho_0 g_i, \tag{68b}$$

$$\frac{\partial \log(\rho_0)}{\partial t} + U_{j0}\frac{\partial \log(\rho_0)}{\partial x_j} = \frac{1}{\mathrm{Sc\,Re}}\nabla^2 \log(\rho_0) \tag{68c}$$

while the divergence constraint at zeroth order is

$$\frac{\partial U_{j0}}{\partial x_j} = -\frac{1}{\mathrm{Sc\,Re}}\nabla^2 \log(\rho_0). \tag{69}$$

Without loss of generality, it is assumed that only the vertical velocity component of the base state is diffusing, such that $\boldsymbol{U}_0 = (0, 0, w_0(z,t))$. By imposing that the velocity decays to zero far from the boundaries, the base state must evolve as

$$\frac{\partial \rho_0}{\partial t} = \frac{1}{\mathrm{Sc\,Re}}\frac{\partial^2 \rho_0}{\partial z^2}, \qquad w_0(z,t) = -\frac{1}{\mathrm{Sc\,Re}}\frac{\partial \log(\rho_0)}{\partial z}, \tag{70}$$

where the density satisfies a diffusion equation, which naturally leads to a self-similar evolution of the base state as reported in Eq.(27).

At first order, the linearized equations are derived by considering the first-order terms in ϵ. In the resulting set of equations, primes are omitted for clarity and are instead reserved for total derivatives with respect to the vertical z direction. Moreover, the QSSA assumption holds, meaning that the base state is frozen and therefore all time derivatives arising from its evolution are omitted.

$$\frac{1}{\rho_0}\frac{\partial \rho}{\partial t} + \frac{1}{\rho_0}\frac{\partial \rho_0}{\partial z} w + \frac{\partial}{\partial z}\left(\frac{\rho}{\rho_0}\right) w_0 = \frac{1}{\mathrm{Sc\,Re}}\nabla^2\left(\frac{\rho}{\rho_0}\right), \tag{71a}$$

$$\rho_0 \frac{\partial u_i}{\partial t} + \rho_0 \frac{\partial w_0}{\partial z} w\,\delta_{i3} + \rho_0 w_0 \frac{\partial u_i}{\partial z} + w_0 \frac{\partial w_0}{\partial z}\rho\,\delta_{i3} = -\frac{\partial p}{\partial x_i} + \frac{1}{Re}\frac{\partial \tau_{ij}}{\partial x_j} - \rho\,\delta_{i3}, \tag{71b}$$

$$\frac{\partial \tau_{ij}}{\partial x_j} = 2\,\mu' S_{i3} + \mu\,\nabla^2 u_i + \frac{1}{3}\mu\,\nabla(\nabla\cdot\boldsymbol{u}) - \frac{2}{3}\mu'(\nabla\cdot\boldsymbol{u})\,\delta_{i3}, \tag{71c}$$

$$\frac{\partial u_i}{\partial x_i} = -\frac{1}{\mathrm{Sc\,Re}}\nabla^2\left(\frac{\rho}{\rho_0}\right). \tag{71d}$$

The vertical component of the momentum equation in Eq.(71b), combined with the divergence of the stress tensor from Eq.(71c), yields

$$\rho_0 \frac{\partial w}{\partial t} + \rho_0 w \frac{\partial w_0}{\partial z} + \rho_0 w_0 \frac{\partial w}{\partial z} + \rho\, w_0 \frac{\partial w_0}{\partial z} = -\frac{\partial p}{\partial z} + \mu\left(\nabla^2 w + \frac{1}{3}\frac{\partial(\nabla\cdot\boldsymbol{u})}{\partial z}\right) + \mu'\left(2\frac{\partial w}{\partial z} - \frac{2}{3}\nabla\cdot\boldsymbol{u}\right). \tag{72}$$

Taking the Laplacian of Eq.(72) yields

$$\begin{aligned}
&\rho''\frac{\partial w}{\partial t} + 2\rho'\frac{\partial}{\partial z}\left(\frac{\partial w}{\partial t}\right) + \rho_0\frac{\partial \nabla^2 w}{\partial t} + \nabla^2\left(\rho_0\frac{\partial w_0}{\partial z}w + \rho_0 w_0\frac{\partial w}{\partial z} + w_0\frac{\partial w_0}{\partial z}\rho\right) = -\frac{\partial(\nabla^2 p)}{\partial z} - \nabla^2\rho \\
&+ \mu\left(\nabla^4 w + \frac{1}{3}\frac{\partial}{\partial z}\left(\nabla^2\nabla\cdot\boldsymbol{u}\right)\right) + \mu'\left(4\frac{\partial \nabla^2 w}{\partial z} + \frac{2}{3}\frac{\partial^2(\nabla\cdot\boldsymbol{u})}{\partial z^2} - \frac{2}{3}\nabla^2\nabla\cdot\boldsymbol{u}\right) \\
&+ \mu''\left(\nabla^2 w + 4\frac{\partial^2 w}{\partial z^2} - \frac{\partial(\nabla\cdot\boldsymbol{u})}{\partial z}\right) + \mu'''\left(2\frac{\partial w}{\partial z} - \frac{2}{3}\nabla\cdot\boldsymbol{u}\right).
\end{aligned} \tag{73}$$

Next, the divergence of the momentum equation in Eq.(71b) followed by differentiation with respect to z leads to the vertical derivative of the Poisson equation,

$$\begin{aligned}\rho_0'' \frac{\partial w}{\partial t} + \rho_0' \frac{\partial}{\partial z}\left(\frac{\partial w}{\partial t}\right) + \rho_0' \frac{\partial \nabla\cdot\boldsymbol{u}}{\partial t} + \rho_0 \frac{\partial}{\partial z}\left(\frac{\partial \nabla\cdot\boldsymbol{u}}{\partial t}\right) + \frac{\partial \Phi(z)}{\partial z} = \frac{\partial(\nabla^2 p)}{\partial z} + \frac{4}{3}\mu \frac{\partial(\nabla^2\nabla\cdot\boldsymbol{u})}{\partial z} - \frac{\partial^2\rho}{\partial z^2} \\ + \mu'\left(\frac{4}{3}\nabla^2\nabla\cdot\boldsymbol{u} + 2\frac{\partial\nabla^2 w}{\partial z} + \frac{2}{3}\frac{\partial^2(\nabla\cdot\boldsymbol{u})}{\partial z^2}\right) + \mu'''\left(2\frac{\partial w}{\partial z} - \frac{2}{3}\nabla\cdot\boldsymbol{u}\right),\end{aligned} \tag{74}$$

where

$$\Phi(z) = \left[\frac{\partial(\rho_0 w_0')}{\partial z} w + \rho_0 w_0' \frac{\partial w}{\partial z} + \frac{\partial(\rho_0 w_0)}{\partial z}\frac{\partial w}{\partial z} + \rho_0 w_0 \frac{\partial(\nabla\cdot\boldsymbol{u})}{\partial z} + w_0 w_0' \frac{\partial\rho}{\partial z} + \frac{\partial(w_0 w_0')}{\partial z}\rho\right]. \tag{75}$$

Substituting Eq.(73) into Eq.(74) leads to

$$\begin{aligned}-\left(\rho_0' \frac{\partial}{\partial z} + \rho_0\nabla^2\right)\frac{\partial w}{\partial t} + \left(\rho_0' + \rho_0\frac{\partial}{\partial z}\right)\frac{\partial(\nabla\cdot\boldsymbol{u})}{\partial t} - \left(\rho_0 w_0'\nabla^2 + w_0\rho_0'\frac{\partial^2}{\partial z^2} + \rho_0 w_0\frac{\partial\nabla^2}{\partial z}\right) w \\ + \frac{\partial(\rho_0 w_0)}{\partial z}\frac{\partial^2(\nabla\cdot\boldsymbol{u})}{\partial z^2} + \rho_0 w_0\frac{\partial^2(\nabla\cdot\boldsymbol{u})}{\partial z^2} - w_0 w_0'\nabla^2_{xy}\rho = \mu\left(-\nabla^4 w + \frac{\partial(\nabla^2\nabla\cdot\boldsymbol{u})}{\partial z}\right) \\ + 2\mu'\left(\nabla^2\nabla\cdot\boldsymbol{u} - \frac{\partial\nabla^2 w}{\partial z}\right) + \nabla^2_{xy}\rho + \mu''\left(\nabla^2 w - 2\frac{\partial^2 w}{\partial z^2} - \frac{\partial(\nabla\cdot\boldsymbol{u})}{\partial z}\right).\end{aligned} \tag{76}$$

The divergence term $\nabla\cdot\boldsymbol{u}$ appearing in Eq.(76) is determined solely by the density perturbation, as derived from Eq.(71d), suggesting that the vertical velocity is solely coupled with the density perturbation.

Defining

$$\nabla\cdot\boldsymbol{u} = -\frac{1}{\mathrm{Sc}\,\mathrm{Re}}\nabla^2\left(\frac{\rho}{\rho_0}\right) = \mathcal{L}_\rho^{\nabla^2}\rho, \tag{77}$$

it is possible to express the system in terms of the differential operators reported in Eq.(28), whose complete definition is reported in the following. In particular, the $\boldsymbol{B}$ matrix in Eq.(29) is defined by

$$\begin{aligned}\mathcal{M}_{ww} &= -\left(\rho_0\frac{\partial}{\partial z} - \rho_0\nabla^2\right), \\ \mathcal{M}_{w\rho} &= \left(\rho_0' + \rho_0\frac{\partial}{\partial z}\right)\mathcal{L}_\rho^{\nabla^2},\end{aligned} \tag{78}$$

while the matrix $\boldsymbol{A}$ in Eq.(28) is defined by

$$\begin{aligned}\mathcal{L}_{w_0 w} &= \left(\rho_0\frac{dw_0}{dz} + \rho_0 w_0\frac{\partial}{\partial z}\right)\nabla^2 + w_0\frac{d\rho_0}{dz}\frac{\partial^2}{\partial z^2}, \\ \mathcal{L}_{w_0\rho} &= -\left(\frac{d(\rho_0 w_0)}{dz}\frac{\partial}{\partial z} + \rho_0 w_0\frac{\partial^2}{\partial z^2}\right)\mathcal{L}_\rho^{\nabla^2} + w_0\frac{dw_0}{dz}\nabla^2_{xy}, \\ \mathcal{L}_{ww} &= \left(-\mu\nabla^4 - 2\mu'\frac{\partial}{\partial z}\nabla^2 + \mu''\nabla^2 - 2\mu''\frac{\partial^2}{\partial z^2}\right), \\ \mathcal{L}_{w\rho} &= \left(\mu\frac{\partial}{\partial z}\nabla^2 + 2\mu'\nabla^2 - \mu''\frac{\partial}{\partial z}\right)\mathcal{L}_\rho^{\nabla^2} - \nabla^2_{xy}, \\ \mathcal{L}_{\rho\rho} &= \mathcal{L}_\rho^{\nabla^2} + \frac{w_0}{\rho_0}\frac{\partial\rho_0}{\partial z} - w_0\frac{\partial}{\partial z}.\end{aligned} \tag{79}$$

These expressions complete the derivation of the velocity–density formulation and establish the operator structure used to construct the incompressible variable-density system.

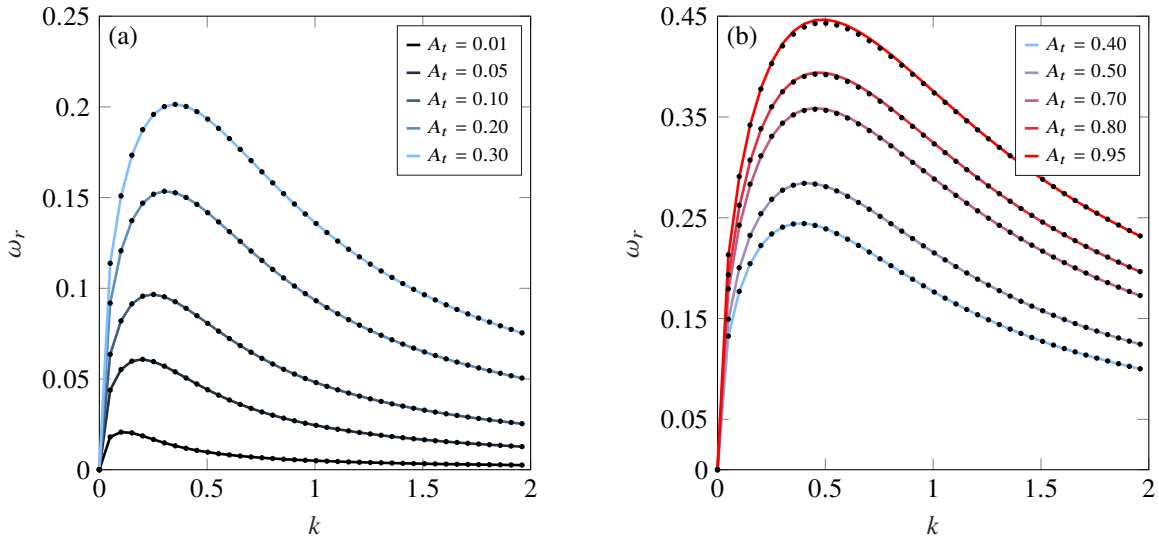

Fig. 6 Verification of the solver against the classical results of Ref. [40]. The comparison illustrates the growth rate of the Rayleigh–Taylor instability in the inviscid limit. (a) Atwood numbers range between 0.01 **and** 0.3**. (b) Atwood numbers range between** 0.4 **and** 0.95**. The symbols represent the results obtained by solving Eq.(81), while the continuous curves represent the results obtained by the solver developed in this work.**

B. Solver Verification

A. Verification I

The solver is first verified against the classical results of Ref. [40]. This initial comparison confirms that the implementation correctly reproduces the canonical Rayleigh–Taylor instability formulation under simplified assumptions. Starting from the general variable-density equations presented in Section IV.A, the model reduces to the inviscid limit considered by Chandrasekhar by setting $1/Sc = 0$ and neglecting viscosity stratification. Under these conditions, the corresponding linear operators simplify to

$$\begin{aligned} \mathcal{L}_\rho^{\nabla^2} &= 0, & \mathcal{M}_{ww} &= -\left(\frac{d\rho_0}{dz}\,\frac{\partial}{\partial z} + \rho_0\,\nabla^2\right), & \mathcal{M}_{w\rho} &= 0, \\ \mathcal{L}_{ww} &= -\tfrac{1}{Re}\,\nabla^2, & \mathcal{L}_{w\rho} &= -\,k^2, & \mathcal{L}_{\rho\rho} &= 0. \end{aligned} \tag{80}$$

The growth rate is obtained by computing the eigenvalues of the discretized operator and selecting the largest real component. The procedure follows the numerical approach detailed previously, ensuring consistency across all test cases. For reference, Ref. [40] determined the growth rate analytically by solving the polynomial equation,

$$y^4 + (1 - A_t^2)\,y^3 + (3\,A_t^2 - 1)\,y^2 - (1 + 3\,A_t^2)\,y + A_t^2 - \frac{A_t}{k^3} = 0, \tag{81}$$

from which the growth rate for each wavenumber k is expressed as

$$\omega_r = \left(y^2 - 1\right) k^2. \tag{82}$$

The theoretical predictions for a sharp interface were reproduced numerically by setting the diffusive layer width to $\delta = 0.025\,L_z$. Fig. 6 compares the present results with Chandrasekhar's analytical predictions and shows excellent agreement across all wavenumbers. Attempts to reduce the diffusive layer thickness while maintaining adequate resolution confirmed that the results remained unchanged, reinforcing the solver's robustness.

B. Verification II

The second Verification compares the results of the present solver with those of Ref. [39], which in turn extends the classical formulation of Ref. [40] to include a finite diffusive layer thickness. The diffusive interface is represented as a

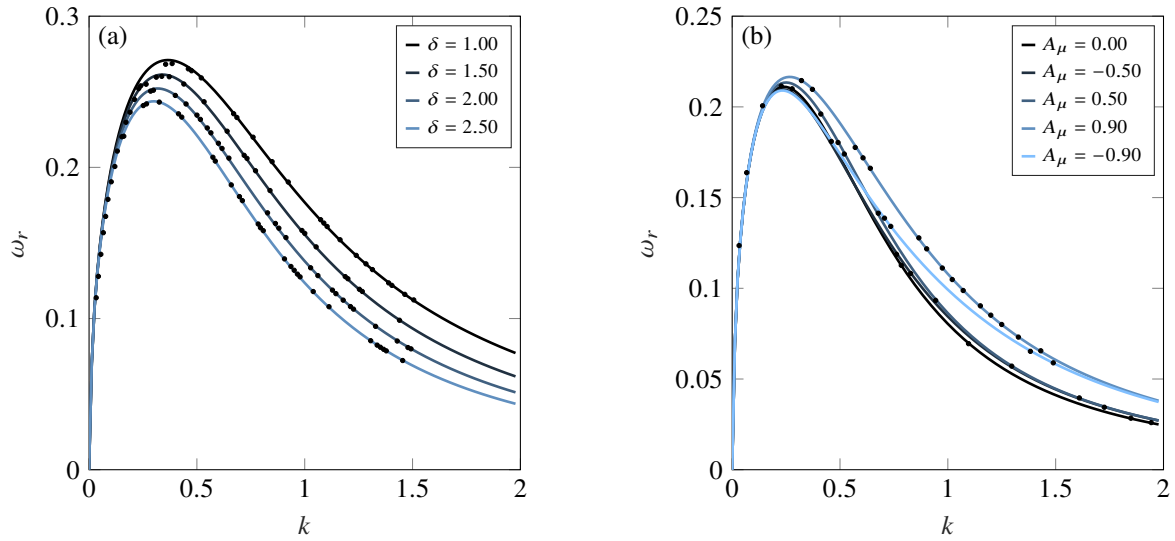

Fig. 7 Verification of the variable-density formulation against the reference results of Morgan et al. [39]. Symbols represent data extracted from the reference study, while continuous lines correspond to the present solver. (a) $A_\mu = 0$ and $A_t = 0.5$ for different layer thicknesses. (b) Case including viscosity stratification at $A_t = 0.5$ and $\delta = 5$. The comparison confirms the solver's accuracy and consistency with established results.

piecewise linear profile, and the eigenvalue problem is solved using the Riccati equation, with matching conditions enforced at the interface through discontinuities in the first derivative. Dynamic diffusion is neglected, eliminating the possibility of species mixing and simplifying the governing equations. Within the present framework, setting $1/Sc = 0$ reproduces the same set of equations, showing that the general formulation of Section IV.A naturally reduces to the equations employed by Ref. [39]. The corresponding operators take the form

$$\begin{aligned} \mathcal{L}_\rho^{\nabla^2} &= 0 & \mathcal{M}_{ww} &= -\left(\rho_0' \frac{\partial}{\partial z} + \rho_0 \nabla^2\right), \\ \mathcal{M}_{w\rho} &= 0 & \mathcal{L}_{ww} &= \left(-\mu \nabla^2 - 2\mu' \frac{\partial}{\partial z} \nabla^2 + \mu'' \nabla^2 - 2\mu'' \frac{\partial^2}{\partial z^2}\right) \frac{1}{Re}, \\ \mathcal{L}_{w\rho} &= -k^2 & \mathcal{L}_{\rho\rho} &= 0. \end{aligned} \tag{83}$$

The first verification case considers $A_\mu = 0$ and $A_t = 0.5$, varying the diffusive layer thickness. The results are presented in Fig. 7a and demonstrate that the solver reproduces the same trends reported in the reference study. The second comparison involves viscosity stratification, which requires additional care. Because the present formulation employs a smooth base-state profile, all viscous derivatives must be retained—unlike in Ref. [39], where a piecewise-linear approximation set higher-order derivatives to zero. Despite this difference, Fig. 7b shows that both formulations yield consistent growth rates, whether or not the viscous terms are explicitly retained.

C. Verification III

The final Verification compares the present formulation with the semi-analytical results of Ref. [41], which extend Chandrasekhar's analysis to finite fluid layers of arbitrary thickness. These results correspond to the classical Rayleigh–Taylor instability problem with discontinuous density and viscosity profiles, defined as

$$\rho(z) = \begin{cases} \rho_1, & -t_1 \le z \le 0, \\ \rho_2, & 0 \le z \le t_2, \end{cases} \qquad \mu(z) = \begin{cases} \mu_1, & -t_1 \le z \le 0, \\ \mu_2, & 0 \le z \le t_2. \end{cases} \tag{84}$$

In this formulation, the quantity

$$q_{1,2}^2 = k^2 + \gamma \frac{\rho_{1,2}}{\mu_{1,2}}, \qquad Q_1 = q_1^2 + k^2, \quad Q_2 = q_2^2 + k^2, \quad \alpha = \frac{g\,k}{\gamma^2}\left(\rho_1 - \rho_2 + \frac{k^2 T^{(s)}}{g}\right), \quad \beta = \frac{2\,k}{\gamma}(\mu_1 - \mu_2) \tag{85}$$

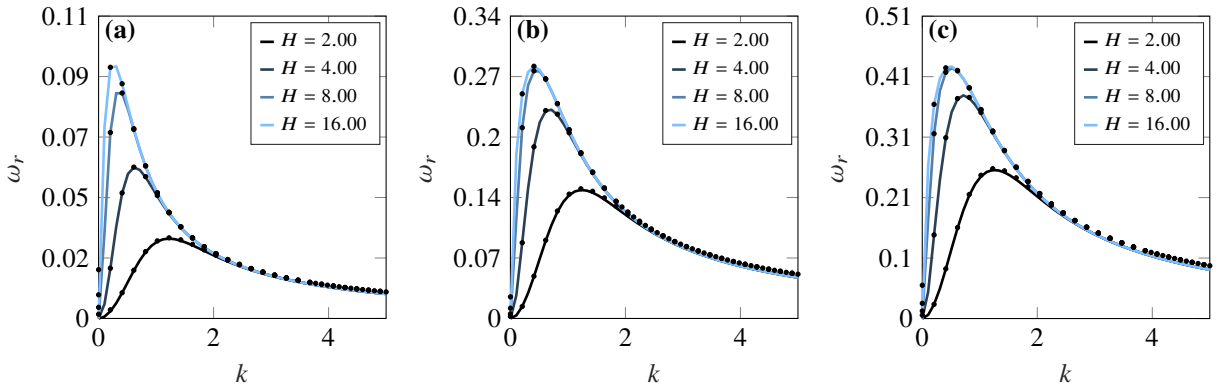

Fig. 8 Comparison between the present solver and the semi-analytical results of Ref. [41] for $A_t = \{0.1, 0.5, 0.9\}$ (a–c) at $A_\mu = 0$. H in the legend denotes the domain height. The symbols represent the results obtained by solving Eq.(87), while the continuous curves represent the results obtained by the solver developed in this work.

arises naturally, leading to the following linear system for the amplitude coefficients,

$$\begin{pmatrix} 1 & 1 & 1 & 1 & -1 & -1 & -1 & -1 \\ k & q_1 & -k & -q_1 & k & q_2 & -k & -q_2 \\ e^{-kt_1} & e^{-q_1 t_1} & e^{kt_1} & e^{q_1 t_1} & 0 & 0 & 0 & 0 \\ 0 & 0 & 0 & 0 & e^{-kt_2} & e^{-q_2 t_2} & e^{kt_2} & e^{q_2 t_2} \\ ke^{-kt_1} & q_1 e^{-q_1 t_1} & -ke^{kt_1} & -q_1 e^{q_1 t_1} & 0 & 0 & 0 & 0 \\ 0 & 0 & 0 & 0 & -ke^{-kt_2} & -q_2 e^{-q_2 t_2} & ke^{kt_2} & q_2 e^{q_2 t_2} \\ 2k^2\mu_1 & Q_1\mu_1 & 2k^2\mu_1 & Q_1\mu_1 & -2k^2\mu_2 & -Q_2\mu_2 & -2k^2\mu_2 & -Q_2\mu_2 \\ \rho_1 + \alpha + \beta k & \alpha + \beta q_1 & -\rho_1 + \alpha - \beta k & \alpha - \beta q_1 & \rho_2 & 0 & -\rho_2 & 0 \end{pmatrix} \begin{pmatrix} A_1 \\ B_1 \\ C_1 \\ D_1 \\ A_2 \\ B_2 \\ C_2 \\ D_2 \end{pmatrix} = \mathbf{0}. \quad (86)$$

In compact notation,

$$\boldsymbol{M}(\gamma, k)\, \boldsymbol{a} = \mathbf{0}, \quad (87)$$

which admits nontrivial solutions when

$$\det\big(\boldsymbol{M}(\gamma, k)\big) = 0. \quad (88)$$

A classical root-finding procedure is applied for each wavenumber to compute the corresponding growth rate in Eq.(87), and the results are compared with those obtained from the present solver. The agreement is evaluated for different Atwood numbers and fluids of the same viscosity, as shown in Fig. 8. Across all configurations, the present solver reproduces the reported trends and magnitudes, confirming the implementation's accuracy and applicability to configurations with finite domain boundaries. In particular, the analysis highlights the influence of the finite vertical domain and shows that when the half-domain height exceeds approximately $H > 16$, the growth-rate curves become nearly insensitive to further increases in domain size.

References

[1] Frame, P., and Towne, A., "Beyond Optimal Disturbances: A Statistical Framework for Transient Growth," *Journal of Fluid Mechanics*, Vol. 983, 2024, p. A2.

[2] Rayleigh, L., "On the Stability, or Instability, of Certain Fluid Motions," *Proceedings of the London Mathematical Society*, Vol. s1-11, No. 1, 1879, pp. 57–72.

[3] Müller, B., "Hydrodynamics of Core-Collapse Supernovae and Their Progenitors," *Living Reviews in Computational Astrophysics*, Vol. 6, No. 1, 2020, p. 3.

[4] Pizzolato, F., and Soker, N., "On the Rayleigh–Taylor Instability of Radio Bubbles in Galaxy Clusters," *Monthly Notices of the Royal Astronomical Society*, Vol. 371, No. 4, 2006, pp. 1835–1848.

[5] Lindl, J., "Development of the Indirect-drive Approach to Inertial Confinement Fusion and the Target Physics Basis for Ignition and Gain," *Physics of Plasmas*, Vol. 2, No. 11, 1995, pp. 3933–4024.

[6] Zhou, Y., "Rayleigh–Taylor and Richtmyer–Meshkov Instability Induced Flow, Turbulence, and Mixing. I," *Physics Reports*, Vol. 720–722, 2017, pp. 1–136.

[7] Meng, J., Zhao, X., Tang, X., Xia, Y., Ma, X., and Gao, D., "Surface Characterization of ICF Capsule byAFM-based Profilometer," *High Power Laser Science and Engineering*, Vol. 5, 2017, p. e21.

[8] Roberts, M. S., and Jacobs, J. W., "The Effects of Forced Small-Wavelength, Finite-Bandwidth Initial Perturbations and Miscibility on the Turbulent Rayleigh–Taylor Instability," *Journal of Fluid Mechanics*, Vol. 787, 2016, pp. 50–83.

[9] Zhou, Y., Williams, R. J. R., Ramaprabhu, P., Groom, M., Thornber, B., Hillier, A., Mostert, W., Rollin, B., Balachandar, S., Powell, P. D., Mahalov, A., and Attal, N., "Rayleigh–Taylor and Richtmyer–Meshkov Instabilities: A Journey through Scales," *Physica D: Nonlinear Phenomena*, Vol. 423, 2021, p. 132838.

[10] Dimonte, G., Ramaprabhu, P., Youngs, D. L., Andrews, M. J., and Rosner, R., "Recent Advances in the Turbulent Rayleigh–Taylor Instability," *Physics of Plasmas*, Vol. 12, No. 5, 2005, p. 056301.

[11] Ramaprabhu, P., Dimonte, G., and Andrews, M. J., "A Numerical Study of the Influence of Initial Perturbations on the Turbulent Rayleigh–Taylor Instability," *Journal of Fluid Mechanics*, Vol. 536, 2005, pp. 285–319.

[12] Livescu, D., Wei, T., and Petersen, M. R., "Direct Numerical Simulations of Rayleigh-Taylor Instability," *Journal of Physics: Conference Series*, Vol. 318, No. 8, 2011, p. 082007.

[13] Dimonte, G., "Dependence of Turbulent Rayleigh-Taylor Instability on Initial Perturbations," *Physical Review E*, Vol. 69, No. 5, 2004, p. 056305.

[14] Thévenin, S., Gréa, B.-J., Kluth, G., and Nadiga, B. T., "Leveraging Initial Conditions Memory for Modelling Rayleigh–Taylor Turbulence," *Journal of Fluid Mechanics*, Vol. 1009, 2025, p. A17.

[15] Schmid, P. J., and Henningson, D. S., *Stability and Transition in Shear Flows*, Applied Mathematical Sciences, Vol. 142, Springer, New York, NY, 2001.

[16] Sandoval, D. L., "The Dynamics of Variable-Density Turbulence," *Ph.D thesis*, 1995.

[17] Daniel, D., Tilton, N., and Riaz, A., "Optimal Perturbations of Gravitationally Unstable, Transient Boundary Layers in Porous Media," *Journal of Fluid Mechanics*, Vol. 727, 2013, pp. 456–487.

[18] Youngs, D. L., "Modelling Turbulent Mixing by Rayleigh-Taylor Instability," *Physica D Nonlinear Phenomena*, Vol. 37, 1989, pp. 270–287.

[19] Kord, A., and Capecelatro, J., "Optimal Perturbations for Controlling the Growth of a Rayleigh–Taylor Instability," *Journal of Fluid Mechanics*, Vol. 876, 2019, pp. 150–185.

[20] Prathama, A. H., and Pantano, C., "Linear Stability Analysis of Two Fluid Columns of Different Densities and Viscosities in a Gravity Field," *Journal of Fluid Mechanics*, Vol. 920, 2021, p. A26.

[21] Livescu, D., and Ristorcelli, J. R., "Buoyancy-Driven Variable-Density Turbulence," *Journal of Fluid Mechanics*, Vol. 591, 2007, pp. 43–71.

[22] Schneider, N., and Gauthier, S., "Asymptotic Analysis of Rayleigh–Taylor Flow for Newtonian Miscible Fluids," *Journal of Engineering Mathematics*, Vol. 92, No. 1, 2015, pp. 55–71.

[23] Weideman, J. A., and Reddy, S. C., "A MATLAB Differentiation Matrix Suite," *ACM Transactions on Mathematical Software*, Vol. 26, No. 4, 2000, pp. 465–519.

[24] Trefethen, L. N., "Is Gauss Quadrature Better than Clenshaw–Curtis?" *SIAM Review*, Vol. 50, No. 1, 2008, pp. 67–87.

[25] Chu, B.-T., "On the Energy Transfer to Small Disturbances in Fluid Flow (Part I)," *Acta Mechanica*, Vol. 1, No. 3, 1965, pp. 215–234.

[26] Schmidt, O. T., Towne, A., Rigas, G., Colonius, T., and Brès, G. A., "Spectral Analysis of Jet Turbulence," *Journal of Fluid Mechanics*, Vol. 855, 2018, pp. 953–982.

[27] Towne, A., Schmidt, O. T., and Colonius, T., "Spectral Proper Orthogonal Decomposition and Its Relationship to Dynamic Mode Decomposition and Resolvent Analysis," *Journal of Fluid Mechanics*, Vol. 847, 2018, pp. 821–867. https://doi.org/10.1017/jfm.2018.283.

[28] Myers, M. K., "Transport of Energy by Disturbances in Arbitrary Steady Flows," *Journal of Fluid Mechanics*, Vol. 226, 1991, pp. 383–400.

[29] Giauque, A., Poinsot, T., Brear, M., and Nicoud, F., "Budget of Disturbance Energy in Gaseous Reacting Flows," ????

[30] Hanifi, A., Schmid, P. J., and Henningson, D. S., "Transient Growth in Compressible Boundary Layer Flow," *Physics of Fluids*, Vol. 8, No. 3, 1996, pp. 826–837.

[31] Holliday, D., and Mcintyre, M. E., "On Potential Energy Density in an Incompressible, Stratified Fluid," *Journal of Fluid Mechanics*, Vol. 107, 1981, pp. 221–225.

[32] Shepherd, T. G., "A Unified Theory of Available Potential Energy 1," *Atmosphere-Ocean*, Vol. 31, No. 1, 1993, pp. 1–26.

[33] Winters, K. B., Lombard, P. N., Riley, J. J., and D'Asaro, E. A., "Available Potential Energy and Mixing in Density-Stratified Fluids," *Journal of Fluid Mechanics*, Vol. 289, 1995, pp. 115–128.

[34] Roullet, G., and Klein, P., "Available Potential Energy Diagnosis in a Direct Numerical Simulation of Rotating Stratified Turbulence," *Journal of Fluid Mechanics*, Vol. 624, 2009, pp. 45–55.

[35] Lamb, K. G., "On the Calculation of the Available Potential Energy of an Isolated Perturbation in a Density-Stratified Fluid," *Journal of Fluid Mechanics*, Vol. 597, 2008, pp. 415–427.

[36] Rapaka, S., Chen, S., Pawar, R. J., Stauffer, P. H., and Zhang, D., "Non-Modal Growth of Perturbations in Density-Driven Convection in Porous Media," *Journal of Fluid Mechanics*, Vol. 609, 2008, pp. 285–303.

[37] Livescu, D., "Numerical Simulations of Two-Fluid Turbulent Mixing at Large Density Ratios and Applications to the Rayleigh–Taylor Instability," *Philosophical Transactions of the Royal Society A: Mathematical, Physical and Engineering Sciences*, Vol. 371, No. 2003, 2013, p. 20120185.

[38] Livescu, D., and Ristorcelli, J. R., "Variable-Density Mixing in Buoyancy-Driven Turbulence," *Journal of Fluid Mechanics*, Vol. 605, 2008, pp. 145–180.

[39] Morgan, R. V., Likhachev, O. A., and Jacobs, J. W., "Rarefaction-Driven Rayleigh–Taylor Instability. Part 1. Diffuse-interface Linear Stability Measurements and Theory," *Journal of Fluid Mechanics*, Vol. 791, 2016, pp. 34–60.

[40] Chandrasekhar, S., *Hydrodynamic and Hydromagnetic Stability*, 1961.

[41] Mikaelian, K. O., "Rayleigh-Taylor Instability in Finite-Thickness Fluids with Viscosity and Surface Tension," *Physical Review E*, Vol. 54, No. 4, 1996, pp. 3676–3680.